Journal of Materials Chemistry C



PAPER

View Article Online
View Journal | View Issue



Cite this: *J. Mater. Chem. C*, 2023, **11**, 4820

Engineering large perpendicular magnetic anisotropy in amorphous ferrimagnetic gadolinium cobalt alloys†

Karthik Srinivasan, (1)** Yulan Chen, (10)* Ludovico Cestarollo, (10)* Darrah K. Dare, Cohn G. Wright and Amal El-Ghazaly (10)**

Amorphous magnetic alloys with large perpendicular magnetic anisotropy (PMA) have emerged as a suitable material choice for spintronic memory and high-frequency non-reciprocal devices on-chip. Unlike ferromagnets, ferrimagnets offer faster switching dynamics, lower net saturation magnetization, minimal stray field and a lower net angular momentum. Ferrimagnetic thin films of Gd_xCo_{1-x} sputter deposited as heterostructures of $Ta/Pt/Gd_xCo_{1-x}(t)/Pt$ on Si/SiO_2 have bulk-like PMA for thicknesses of 5–12 nm and room-temperature magnetic compensation for x=28-32%. Preferential oxygenation of GdCo has been found to increase the effective anisotropy energy density by an order of magnitude and produce near-ideal remanence ratios. X-ray photoelectron spectroscopy accurately quantifies the metal-oxidation ratio, which shows that an oxygen-rich and Co-deficient stoichiometry ($Gd_{21}Co_{28}O_{51}$) likely weakens the ferromagnetic exchange interaction between Co-Co and contributes additional antiferromagnetic exchange through superexchange-like interactions between Gd and Co *via* O, resulting in a stronger out-of-plane magnetization. Even greater PMA and giant-anisotropy field of 11 kOe are achieved in super-lattices of the $Gd_{21}Co_{28}O_{51}$ heterostructure. The combination of ferrimagnetic ordering in amorphous Gd_xCo_{1-x} and its affordance of pathways for engineering large PMA will enable the design of integrated high-frequency devices beyond 30 GHz and ultrafast energy efficient memory devices with switching speeds down to tens of picoseconds.

Received 27th January 2023, Accepted 18th March 2023

DOI: 10.1039/d3tc00332a

rsc.li/materials-c

Introduction

Amorphous ferrimagnetic alloys provide the ease of fabrication and processing and the strong exchange anisotropy necessary for integrated magnetic memories and high frequency devices. In particular, for magnetic random-access memory (MRAM), materials with perpendicular magnetic anisotropy (PMA) are preferred over in-plane magnets owing to high thermal stability in scaled-down dimensions. ^{1–4} An advantage of ferrimagnetic materials, such as those explored in this work, is that they still provide a distinct net moment, making it possible to detect their magnetization state, and much faster switching speeds can be achieved if large PMA is engineered in these materials. ⁵ Similarly, non-reciprocal devices such as circulators and isolators

In this regard, the attractive physical properties of amorphous rare-earth (RE)-transition metal (TM) ferrimagnetic alloys and their ease of processing, makes them ideal materials choices for both MRAM and non-reciprocal high-frequency devices. $^{10-14}$ Amorphous alloys containing TM elements (Fe, Co and Ni) and RE elements (Gd, Tb etc.) have antiparallel coupling due to exchange interactions between the d and f electrons even in the absence of a crystalline order. 13,15 Varying the RE-TM atomic ratio controls the net magnetization and, for a certain composition (or temperature; $T_{\rm M}$), the net magnetization approaches a compensated state ($M_{\rm S}\approx 0$), where the total angular momentum also approaches zero. $^{16-18}$ As mentioned, the stiff negative exchange interaction in ferrimagnets provides the added benefits of high anisotropy energy density, reduced stray fields and

benefit from the microwave/mm-wave operation afforded by the large anisotropy of ferrimagnetic materials, but have historically only been available in bulk form and have required a high-temperature annealing processes to get the desired properties.^{6–8} Furthermore, an engineered PMA in thin-film ferrimagnetic devices provides the asymmetric permeability tensor with isotropic in-plane permeability necessary for the integration of microwave and mm-wave devices and an opportunity to break inversion symmetry to establish non-reciprocity.⁹

^a Department of Electrical and Computer Engineering, Cornell University, 116 Hoy Road, 114 Phillips Hall, Ithaca, New York 14853, USA.

E-mail: ks934@cornell.edu, ase63@cornelledu

b Department of Materials Science and Engineering, Cornell University, 116 Hoy Road, 114 Phillips Hall, Ithaca, New York 14853, USA

^c Cornell Center for Materials Research, Cornell University, 627 Clark Hall of Science, Ithaca, New York 14853, USA

[†] Electronic supplementary information (ESI) available. See DOI: https://doi.org/ 10.1039/d3tc00332a

improved resistance to external field perturbations. Additionally, the amorphous nature of these alloys makes it possible to integrate them monolithically without a high-temperature process. The desired strength of bulk-like PMA in heavy-metal/ferrimagnet heterostructures can be controllably designed for by varying the composition. In the case of a multi-repetition stack of RE-TM layers, an additional control knob for the anisotropy exists by varying the inter-layer dipolar interactions.

In this paper, we engineer a large perpendicular magnetic anisotropy in Gd_xCo_{1-x} alloys and define pathways to tune the magnetic anisotropy through variations in alloy stoichiometry, incorporation of oxygen and multi-repetition heterostructures. Gd_xCo_{1-x} is selected for a few reasons: (i) specific compositions of GdCo have a roomtemperature magnetic compensation (or low total angular momentum), 19 (ii) ultrafast magnetization dynamics and domain wall velocities >1 km s⁻¹ are observed^{13,14,20,21} and (iii) effective fields from SOT being at least an order of magnitude greater than other RE-TM alloys like CoTb or CoFeGd. 12,22-24 PMA in Gd₂Co_{1-x} is a necessity if it is to be considered for the storage layer in MRAM or a bias-free microwave circulator, and it is typically achieved through heterostructures of heavy-metal (Pt and Ta)/ferrimagnetic layers. 14,19

However, several reports have shown that due the large negative enthalpy of RE for oxide formation, Gd in Gd_xCo_{1-x} is prone to oxidation and consequently poor magnetic properties when capped with an oxide layer or a metal that tends to oxidize from high-temperature annealing. 19,25,26 On the contrary, a few reports have instead shown an enhancement in PMA when reactive gases such as N2 or O2 are introduced in trace quantities. 27-30 S. Esho showed that Gd_xCo_{1-x} films sputtered with a partial pressure of N₂ had better perpendicular anisotropy but a saturation magnetization that exhibited a steep dependence on the temperature about the compensation point.27 Similarly, Brunsch and Schneider showed that Gd_xCo_{1-x} with an in-plane anisotropy develops a partial outof-plane component when the alloy has a 15% atomic fraction of O_2 . However, large dM/dT and mixed anisotropies (weak PMA) in the magnetic layer are unsuitable for applications relying on SOT switching (or maximum torque) and isotropic in-plane permeability. Therefore, through this work, we clarify the RE-TM chemistry and demonstrate that strong, wellcontrolled PMA is possible for a variety of Gd/Co compositions. Reactive oxygenation, which would have been deemed detrimental to RE cations, is instead shown to enhance PMA by at least an order of magnitude at a composition of $Gd_{21}Co_{28}O_{51}$. Lastly, strong dipolar coupling is engineered in multi-repetition heterostructures of GdCo whose anisotropy fields are greater than 11 kOe and gyromagnetic resonance frequencies exceed 30 GHz, corresponding to switching rates of less than 30 ps.

Results and discussion

Heterostructure engineering and Gd/Co composition dependence on PMA

Polycrystallinity of the PMA heterostructure. Thin films containing Ta(3 nm)/Pt(3 nm)/Gd_xCo_{1-x}(t)/Pt(5 nm) were sputter-deposited on

 $Si/SiO_2(3 \text{ nm})$ substrates using Ar gas. The $Gd_xCo_{1-x}(t)$ layer, in particular, was reactively sputtered in an ambient environment of Ar and a partial pressure of O2 with a flow rate of 0.5 sccm. The composition of the Gd_xCo_{1-x} alloy was varied by changing the sputtering power for Gd target between 20-50 W, while maintaining the Co target at a constant power of 50 W. The thickness of the magnetic layer ranged from 4-12 nm depending on the sputter yields for the different compositions. PMA in Gd_xCo_{1-x} is contingent upon the crystallinity of the underlying heavy-metal layer, which in this case is a 3 nm thick Pt. Polycrystallinity is measured from both intensity and the fullwidth half maximum (FWHM) of the Pt(111) diffraction peak centered at 39.6°. A higher intensity and narrower FWHM of the Pt(111) peak indicates desired crystallinity and a low degree of crystalline disorder. X-ray diffraction (XRD) spectra in Fig. 1(a) shows the degree of Pt crystallinity for different underlayers of Ta and SiO₂; increased (poly-) crystallinity (narrow FWHM) in Pt was obtained when the underlying Ta had an optimal thickness of 3 nm. Similarly, the thickness of SiO2 also affects the polycrystallinity of the heavy-metal layers, which can affect the magnetic anisotropy of Gd_rCo_{1-r} . A sensitive balance exists between the polycrystallinity of the underlying layers and the anisotropy of the Gd_xCo_{1-x} as shown in Fig. S1 (ESI†). The inclusion of a 3 nm SiO₂ to the underlayer (Si/SiO₂/Ta/Pt), further improves the remanence ratio $(M_R/M_S \approx 1)$ in Gd_xCo_{1-x} compared to films deposited on pristine Si substrates (Si/Ta/Pt underlayers), where $M_R/M_S < 0.75$ or a thicker SiO₂ (6 nm), where $M_{\rm R}/M_{\rm S} < 0.1$ as shown in Fig. 1(b) and (c) and in Fig. S2 of the ESI,† respectively.

Composition dependence on magnetic properties and PMA in Gd_xCo_{1-x} . The ferrimagnetic ordering of the RE and TM moments facilitates the modulation of the magnetic properties of the GdCo alloy through changes in stoichiometry. Compositional analysis carried out using energy dispersive X-ray spectroscopy (EDS) in Fig. 2(a) (and Fig. S3, ESI† with oxygen) shows that the atomic fraction of Gd increases with the sputtering power and decreases when the sputtering power is > 45 W. This latter case suggests that, at high powers, the metal oxidation rate of the target surface is greater than the sputter rate in a reactive process, resulting in Gd-deficient compositions at higher sputtering powers. It is worth noting that the EDS error margin is ± 5 to 8% and the reactive oxygen flow rate is kept constant at 0.5 sccm; the role of oxygen will be discussed in subsequent paragraphs.

Magnetic characterization using a vibrating sample magnetometer (VSM) as shown in Fig. S4 (ESI†) reveals a room temperature compensation (at 300 K) for a Gd composition between x = 28% to 32% $(X_{\rm M})$, where the saturation magnetization approaches zero as seen in Fig. 2(b). Another characteristic of the compensation point is a diverging coercivity, which is usually attributed to a single domain like behavior where the magnetization reversal process happens through coherent rotation.³¹ However, the data in Fig. 2(b) shows that a large coercivity occurs for a narrow composition range of 20-25 Gd At%, which is below the magnetic compensation window. The MH measurements for samples in that composition range show that at lower Gd

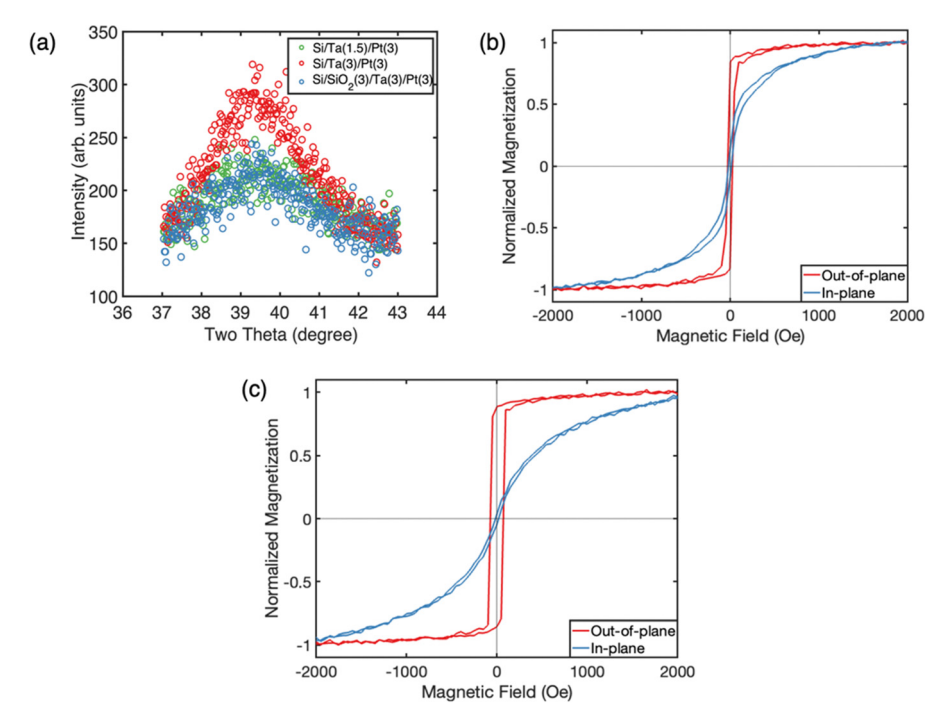


Fig. 1 Role of Pt crystallinity and SiO₂ in PMA Heterostructure. (a) X-ray diffraction spectra of polycrystalline Pt (111) sputtered on combinations of Ta and SiO_2 underlayers with different thicknesses. (b) Hysteresis measurements of Gd_xCo_{1-x} heterostructure deposited on Si substrates without SiO_2 showing a lower remanence ratio and anisotropy field. (c) Hysteresis measurements of Gd_xCo_{1-x} heterostructure deposited on $Si/SiO_2(3 \text{ nm})$ with larger remanence ratio and anisotropy field.

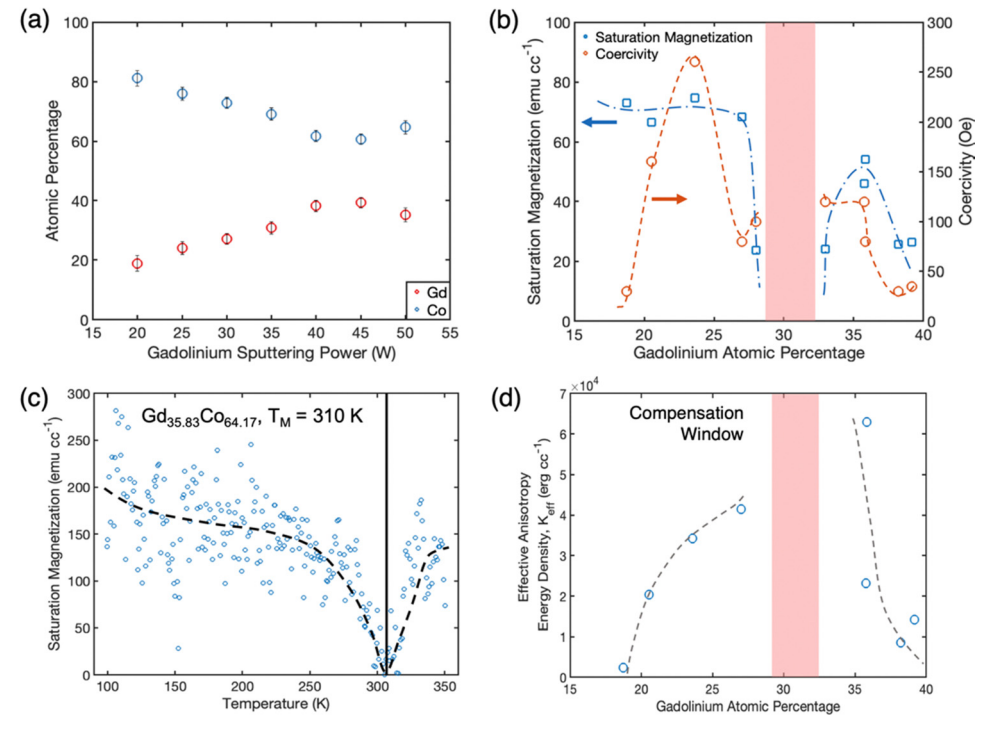


Fig. 2 Effect of Gd Composition on PMA in partially oxidized Gd_xCo_{1-x} . (a) Atomic percentages of Gd and Co for different Gd sputtering powers obtained through energy dispersive X-ray spectroscopy (EDS). The error bars correspond to one standard deviation from an average of 9 measurements. (b) Compositional dependence of saturation magnetization and coercivity of Gd_xCo_{1-x} thin films. The compensation window between 28–32 Gd At% is indicated by the shaded region. (c) Temperature-dependent magnetization measurement of a Gd-rich alloy ($Gd_{35.83}Co_{64.17}$) at H=1400 Oe shows a compensation temperature of 310 K. (d) Effective anisotropy energy density for different Gd atomic fractions calculated from the corresponding hysteresis measurements shows a divergence about the compensation window. Dashed lines in panels (b) - (d) are for visualization of the relevant trends. The films here are sputtered with 0.5 sccm of oxygen and are partially oxidized.

concentrations, the two magnetic sub-systems (Gd and Co) in the alloy undergo magnetization reversals with two distinct coercive fields resulting in a bow-tie shaped hysteresis loop (Fig. S4(d), ESI†). This suggests that when Gd is introduced in a Corich amorphous matrix, there is a certain composition threshold below which the two cations tend to exist as distinct domains, and only at higher Gd compositions does the alloy phase dominate the magnetization reversal process. On the other hand, the lack of a diverging coercivity at the compensation point remains an open question and requires additional temperature-dependent measurements to be fully understood but are outside the scope of the current discussion.

Other researchers have observed a compensation point between x = 21-26% in Gd_xCo_{1-x} synthesized without oxygen. ^{18,19} In the oxygen-containing compositions reported in this paper, the oxidation of the Gd and Co cations reduces their respective magnetic moments, and for Gd-rich (or Co-deficient) compositions (x > 32), $T_{\rm M} > 300$ K, and for Gd-deficient (or Co-rich) compositions (x < 28), $T_{\rm M} < 300$ K. Fig. 2(c) shows the temperature dependent magnetization in a Gd-rich alloy that has a compensation temperature of 310 K (above room temperature) and a weak temperature dependence in the 100 K-250 K range owing to the oxidation of some of the Gd cations.

The hysteresis measurements (MH) at 300 K in Fig. S4 (ESI†) show that thin-film heterostructures of Gd_xCo_{1-x} for Gd compositions between x = 18-39% have PMA. For an MH measurement with n number of field steps, the equation below describes how the effective anisotropy energy density can be calculated from the difference in area under the easy and hard axis MH curves in the first quadrant.

$$K_{\text{eff}} = \sum_{n=0}^{\text{saturation}} \left[\frac{M(n) + M(n+1)}{2} \times [H(n+1) - H(n)] \right]_{\text{OOP}}$$
$$- \sum_{n=0}^{\text{saturation}} \left[\frac{M(n) + M(n+1)}{2} \times [H(n+1) - H(n)] \right]_{\text{IP}}$$
(1)

Further, the uniaxial anisotropy energy density (K_u) is expressed as the sum of the effective anisotropy and the shape anisotropy (assuming a thin film with demagnetization factor of 4π),

$$K_{\rm u} = K_{\rm eff} + 2\pi M_{\rm S}^2 \tag{2}$$

Effective anisotropy calculated from the relations of anisotropy field (H_K) and saturation magnetization (M_S) , where $K_{\text{eff}} =$ $(H_k M_s)/2$, overestimates the anisotropy energy density by assuming a near-ideal hard-axis hysteresis behavior. The areamethod accounts for non-ideal hard-axis curves and provides an accurate measure of the anisotropy energy density. Fig. 2(d) shows that K_{eff} increases with Gd atomic fraction and is positive for all Gd_xCo_{1-x} compositions. For Gd atomic percentage > 36, the anisotropy energy density decreases, likely from excessive RE-oxidation at higher sputtering powers. While K_{eff} is not calculated for samples in the compensation window due to poor signal to noise ratio in the MH measurements, a large K_{eff}

(and strong PMA) is observed in slightly Gd-rich compositions at $x > X_{\rm M}$. However, the stark contrast in the effective anisotropy of samples having similar Gd compositions (35.78% and 35.83%) sputtered at 35 W and 40 W, respectively, could be a consequence of varying extent of cation oxidation in the alloy. This disparity in anisotropy motivates the need to understand the role of oxygen as elucidated in the following section.

Role of oxygen incorporation on PMA in $Gd_{35-x}Co_{65-y}O_{x+y}$

Magnetic properties of $Gd_{35-x}Co_{65-y}O_{x+y}$. The role of oxygen in Gd_xCo_{1-x} alloys has been contradictory in the literature, where it is either discussed as a detriment to the RE cation or a benefit to the PMA in the alloy. 25-28 Even in the report that proposes the latter, only partial PMA is achieved with trace amounts of oxygen, precluding them from being used for SOT devices.28 A thorough consideration of reactive oxygen is lacking. Considering the practical difficulties in regulating trace O2 composition in partially-oxidized Gd_xCo_{1-x} , this work particularly focuses on the role of sub-1 sccm O2 flow rates in a reactive sputtering process, which can be achieved using a standard mass flow controller (MFC). While the oxygen content was regulated using the MFC, the argon flow rate and Gd (35 W)/ Co (50 W) sputtering powers are held constant. This ensures that the resulting variation in oxygen content in the thin film is independent of any variation in the Gd and Co content in the film and their affinities to oxygen. The MH measurements (Fig. 3(a) and (b)) of Gd₃₅Co₆₅ heterostructures sputtered in a reactive ambient of O2 reveal that PMA with a large remanence ratio $(M_R/M_S > 0.95)$ is obtained for an optimal flow rate of 0.5 sccm, while samples sputtered at 0.3 and 0.8 sccm of O₂ had weaker PMA and a smaller remnant magnetization $(M_R/M_S <$ 0.4). Furthermore, an increase in oxygen flow rate decreases the saturation magnetization due to excessive oxidation of the Gd and Co in the alloy. The effective anisotropy energy densities $(K_{\rm eff})$ calculated from the hysteresis measurements shows that $K_{\rm eff}$ increases to 1 \times 10⁵ erg cc⁻¹ at 0.5 sccm O₂, an order of magnitude greater than the K_{eff} for a sample sputtered without O2 and decreases for higher oxygen flow rates, as shown in Fig. 3(c). The hysteresis measurements with an extended range of the magnetic field (between +5 kOe and -5 kOe), are shown in Fig. S5 and S6 (ESI†), and a summary of effective anisotropy energy and in-plane saturation fields are provided in Table S1 (ESI†).

Characterization of oxygen using X-ray photoelectron spectroscopy. It is evident that for excessive O₂ flow rates, the RE and TM oxidize, deteriorating the PMA and magnetization in Gd_xCo_{1-x} heterostructures. However, it is worth exploring the cation to oxygen ratio that favors PMA at the optimal 0.5 sccm flow rate and the mechanism for the increase in anisotropy with increasing O2 flow rate up to 0.5 secm. X-ray photoelectron spectroscopy (XPS) and ion milling are used in conjunction to examine the binding energies of the Gd, Co and O in the $Gd_{35-x}Co_{65-y}O_{x+y}$ layer of the thin-film heterostructure. For a sample deposited at 0.3 sccm O2, high-resolution XPS spectra shown in Fig. 4(a)-(c) reveals a Gd: Co ratio of 1:2, and a cation to oxygen (R:O) ratio of 64:36, which results in a

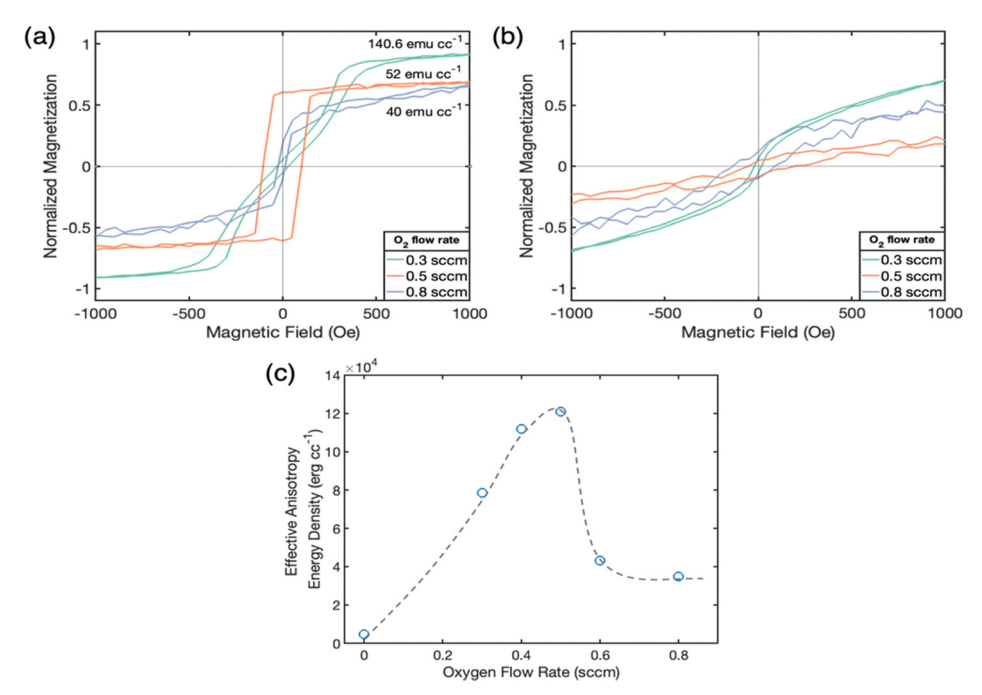


Fig. 3 Role of reactive O_2 in the PMA of $Gd_xCo_yO_{1-x-y}$. (a) Out-of-plane hysteresis measurements from Gd_xCo_{1-x} samples sputtered with different oxygen flow rates. The saturation magnetization is normalized to the largest value to represent the gradual decrease due to oxygen flow. (b) In-plane hysteresis measurements from the same samples show clear preference to perpendicular magnetization. (c) Variation of effective anisotropy energy density with oxygen flow rate indicates an optimal flow rate where the anisotropy is maximum.

stoichiometry of $Gd_{21}Co_{43}O_{36}$. The $Gd\ 4d_{5/2}$ and $4d_{3/2}$ core-level transitions are fit with two asymmetric Lorentzian peaks (at 141.4 and 148.2 eV) that are constrained in their areas according to the d-shell spin-orbit splitting, and an additional peak at

144 eV for the oxide that appears as a shoulder to the $4d_{5/2}$ peak. On the other hand, the 2p_{3/2} peak is fit for Co using an asymmetric Lorentzian with an exponential tail (at 777.9 eV) and a phonon loss peak at 783.4 eV. The Co oxide peak is

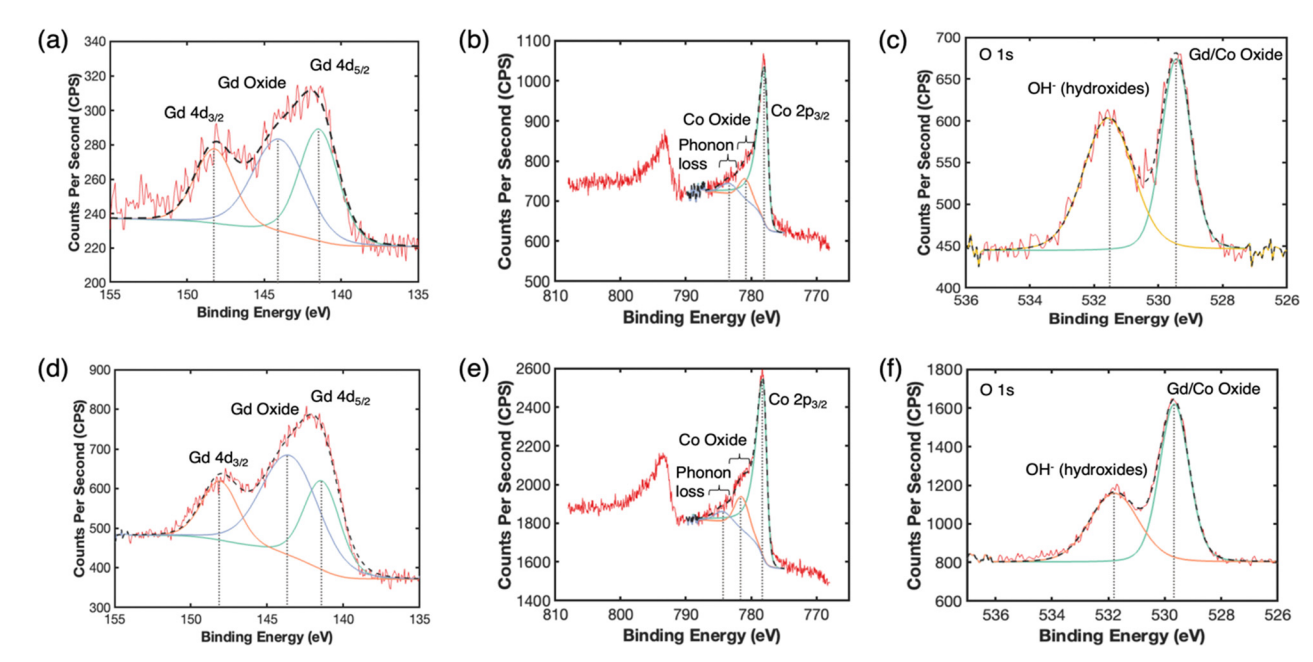


Fig. 4 XPS analysis of reactive O_2 in $Gd_xCo_yO_{1-x-y}$. High-resolution XPS spectra for Gd 4d, Co 2p and O 1s peaks from samples sputtered with 0.3 sccm of O_2 in panels (a)–(c) and with 0.5 sccm of O_2 in panels (d)–(f). The key difference in the peak-ratios for the different oxygen flow rates can be observed in panels (c) and (f). The vertical dashed lines and corresponding labels indicate the peaks and the positions of the hybrid Gaussian-Lorentzian profiles used to fit the spectra.

typically found at energies greater than the core-level peak, and here, this is modelled using a peak at 780.8 eV, with a difference of 2.9 eV from the 2p_{3/2} peak.³²⁻³⁴ Oxidation of the cations also decreases the binding energy of oxygen, and this is seen in the O 1s peak at 529.4 eV (Δ = 1.6 eV from elemental O 1s peak), which corresponds to oxides of both Co and Gd, while the higher energy peak at 531.6 eV is attributed to a nonstoichiometric hydroxyl group bonded to Gd. 35,36 While it is not possible to deconvolute the contributions of Gd and Co oxides from the O 1s peak, the XPS spectra of Gd and Co indicate that a larger fraction of Gd is oxidized compared to Co. Although the samples are capped with a protective 5 nm Pt layer which prevents surface OH⁻¹ adsorption after deposition, it is possible that some water vapor might enter the deposition chamber from the load lock during sample transfer due to imperfect vacuum conditions. Full range survey spectra of the XPS measurements are shown in Fig. S7 in the ESI.†

Similarly, at a higher flow rate of 0.5 sccm, as shown in Fig. 4(d)-(f), the Gd: Co ratio is 3:4 and the R:O ratio is 1:1, with an oxygen-rich stoichiometry of Gd₂₁Co₂₈O₅₁. The peak positions and the full width at half maximum intensity (FWHM) for the different Gd, Co and O peaks are given in Table 1. Here, in addition to the expected cation oxidation, a larger fraction of Co is oxidized in comparison to the sample sputtered at 0.3 sccm O2 flow rate. A higher oxidation fraction of cations can be seen from the XPS spectra for O 1s (Fig. 4(f)), where the peak at 529.7 eV corresponding to Gd/Co oxide is prominent compared to the peak for the hydroxide at 531.8 eV. Preferential oxidation of cobalt at higher oxygen flow rates is likely due to DC magnetron sputtering of cobalt (as opposed to the RF magnetron sputtering of gadolinium), which lacks the alternating RF voltage that deoxidizes the target every half cycle. Comparison of atomic fractions of Gd, Co and O obtained from XPS spectra for the samples sputtered at 0, 0.3, and 0.5 sccm O₂ flow rates shows that the Gd atomic fraction remains constant, while the Co atomic fraction decreases commensurately with higher oxygen flows. This is also reflected in the stoichiometry at higher oxygen flow rates, which is cobalt deficient due to reduced sputter yield. Interestingly, the atomic fraction of hydroxide remains constant about 19-21% across samples sputtered at 0, 0.3 and 0.5 sccm of O₂ flow (Table S2 in ESI†), indicating that hydroxyl contamination is independent of the reactive flow rates. A summary of the binding energies in the RE-TM metals and oxides for the different oxygen flow rates is given in Table 1.

The role of oxygen in the PMA of Gd_xCo_{1-x} is further illustrated in Fig. S8 (in the ESI†) through two cases of Gd₃₅Co₆₅ sputtered at a lower O2 flow rate of 0.3 sccm, but from targets that are either (i) pristine and metallic or (ii) partially oxidized. The films sputtered from metallic targets with sub-optimal O2 flow rates have a weak PMA ($K_{\rm eff} = 7.8 \times 10^4 \, {\rm erg \ cc^{-1}}$) and small remanence ratio ($M_R/M_S = 0.15$), as shown in Fig. S8(a) (ESI†). However, the films sputtered from targets exposed (or "seasoned") to 5 mTorr of O2 for 60 s prior to reactive sputtering, demonstrate a strong PMA ($K_{\rm eff} = 1.7 \times 10^5 \ {\rm erg \ cc^{-1}}$) with a remanence ratio (M_R/M_S) of 0.75, as shown in Fig. S8(b) (ESI†). This implies that at specific oxygenation ratios (R:O), strong PMA is possible.

Superexchange-like interactions in Gd-O-Co. PMA in $Gd_xCo_yO_{1-x-y}$ can be understood by considering the structure and the different exchange interactions between the RE-TM cations and the oxygen anion. Previous works have shown that oxidation of Gd_xCo_{1-x} results in a structural transformation from an amorphous alloy to amorphous oxide. 37,38 Here, XRD spectra (Fig. S9, ESI†) from GdCoO shows that the alloys are amorphous for all oxygen flow rates, which means the magnetic properties are a consequence of the exchange interactions in the absence of a long-range structural order. In pure GdCo (non-oxygenated), the exchange energies J_{Gd-Gd} and J_{Co-Co} for the Gd-Gd and Co-Co dipolar interactions, respectively, are positive, denoting a ferromagnetic alignment, while the $J_{\text{Gd-Co}}$ energy for the Gd-Co dipolar interaction is negative, denoting an antiferromagnetic alignment. 39-41 However, with the introduction of oxygen, additional interactions such as the superexchange-like coupling between the magnetic cations (R:Gd,Co) via the non-magnetic anion (O) must be taken in to consideration. Then, the net exchange interaction in the material system can be represented as a sum of all possible dipolar interactions, as shown in eqn (3).

$$J_{\text{ex}} = J_{\text{Gd-Gd}} + J_{\text{Gd-Co}} + J_{\text{Co-Co}} + J_{\text{Gd-O-Gd}} + J_{\text{Gd-O-Co}} + J_{\text{Co-O-Co}}$$
(3)

The first three are those of pure GdCo and result in an effective exchange energy that is negative and represents antiparallel orientation that is perpendicular to the plane of the film; the latter three arise when oxygen is introduced to the film. Usually, the exchange energies corresponding to Gd-Gd (and Gd-O-Gd) interactions are much smaller than those of Gd-Co or Co-Co pairs and can be ignored from further consideration. In the presence of oxygen, XPS measurements

Table 1 Summary of binding energies for Gd, Co and RE-TM oxides

| ${ m O_2}$ flow rate (sccm) | Binding energies (eV) and full width at half maximum intensity; FWHM ^a (eV) | | | | | | | |
|-----------------------------|--|---|--|---|---|-------------------------------------|--|--|
| | Gd 4d | | | Co 2p | | | O 1s | |
| | Gd 4d _{5/2} | Gd 4d _{3/2} | Gd oxide | Co 2p _{3/2} | Co oxide | Co phonon loss | Gd/Co oxide | ОН |
| 0 0.3 0.5 | 141 (2.7) 141.4 (2.98) 141.4 (2.82) | 147.7 (2.7) 148.2 (2.98) 148 (2.82) | 143.3 (4.01) 144 (4.04) 143.5 (4.42) | 777.8 (1.2) 778 (1.25) 778.2 (1.36) | 780.3 (1.9) 780.9 (2.31) 781.4 (2.63) | 782.5 (3) 783.4 (3) 784.3 (3) | 529.2 (1.05) 529.4 (1.07) 529.7 (1.24) | 531.4 (2.02) 531.6 (1.82) 531.8 (2.04) |

^a The FWHM is given in the parentheses.

indicate that Co is preferentially oxidized and that the alloys are Co-deficient, both of which signify a weaker (or less positive) $J_{\text{Co-Co}}$, and stronger (or more negative) $J_{\text{Gd-O-Co}}$ and $J_{\text{Co-O-Co}}$. Ignoring the weak contributions of Gd-Gd interactions, the effective exchange energy is larger and negative, suggesting a strong PMA in the oxygenated alloy $\text{Gd}_x\text{Co}_v\text{O}_{1-x-v}$.

Ultra-high anisotropy in multi-repetition heterostructures

The largest anisotropy energy density that is obtained through variations in composition and reactive oxygen flow is 1×10^5 erg cc⁻¹, with an anisotropy field (H_k) of 3.3 kOe that corresponds to an operating frequency under 10 GHz. In order to achieve ultrafast switching speeds or microwave/mm-wave operation, an anisotropy field at least three times greater is required. The pathways for increasing the anisotropy field usually rely on the crystalline structure (or growth along a crystallographic direction), or magnetoelasticity. However, the lack of crystalline order in amorphous Gd_xCo_{1-x} alloys means that long-range isotropic order or strong magnetocrystalline anisotropy is not possible. Moreover, amorphous Gd_xCo_{1-x} has a smaller magnetostriction constant ($\lambda_s = 8.34 \times 10^{-6}$) than other soft ferrites (such as garnets or spinels), resulting in weak magnetoelastic anisotropy. 42,43 Therefore, neither magnetocrystalline nor magnetoelastic anisotropy, can be utilized here to amplify the PMA in Gd_xCo_{1-x} .

Multi-repetition heterostructures are a feasible way to increase the anisotropy field, which, in this case, sees a large

contribution from the strong dipolar coupling between the magnetic layers. Similar approaches have been implemented with Co and CoFeB, but the critical thickness for PMA in a single layer (typically around 1 nm in thickness) prevents the overall heterostructure from having a large magnetic volume fraction. 44,45 Here, $Gd_{21}Co_{28}O_{51}$ (11 nm) with bulk like PMA are deposited as super-lattices with up to 10 repetitions of the heterostructure unit cell ([SiO₂(3 nm)/Ta(3 nm)/Pt(3 nm)/ $Gd_{21}Co_{28}O_{51}(11 \text{ nm})/Pt(5 \text{ nm})|_{n}$). Fig. 5(a) and (b) shows that the saturation field (including the effect of shape anisotropy) for the in-plane loop increases with the number of repetitions in the super-lattice and approaches 15 kOe for n = 10. The effective anisotropy energy density in Fig. 5(c) shows that K_{eff} increases by an order of magnitude in the heterostructure with 10 repetitions compared to a single heterostructure. The effective anisotropy energy density (K_{eff}) for n = 10 is 2.13×10^5 erg cc⁻¹, which results in an anisotropy field (excluding shape anisotropy) of 11 kOe for a saturation magnetization (M_S) of 42 emu cc⁻¹. This corresponds to a ferromagnetic resonance (FMR) frequency exceeding 30 GHz, and a switching speed less than 30 ps, which is significantly faster than currently researched ferromagnets.

Conclusions

In summary, three distinct pathways are explored to improve perpendicular magnetic anisotropy in heterostructures of

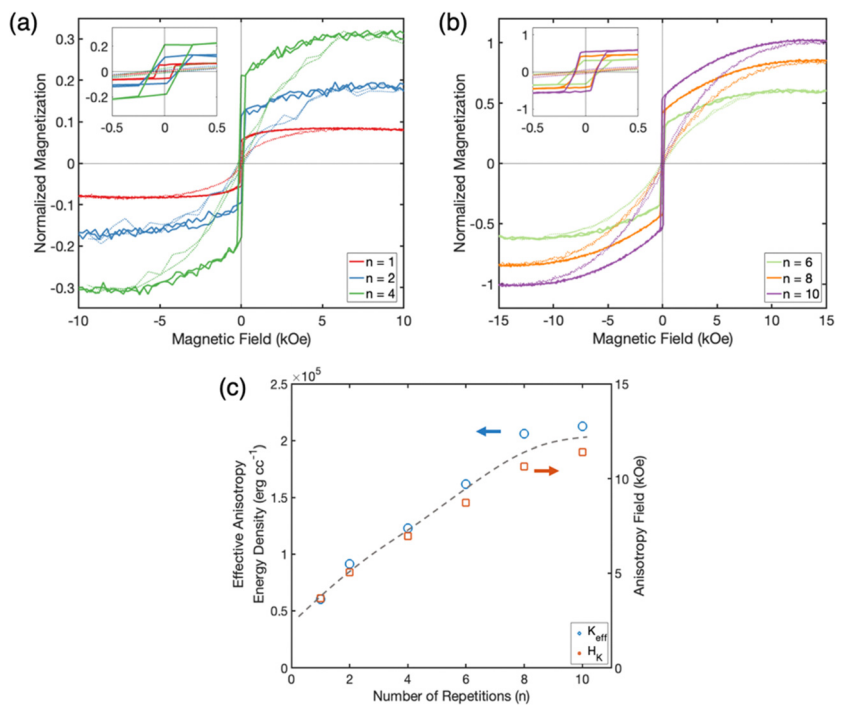


Fig. 5 Large anisotropy fields from PMA heterostructure super-lattices. Hysteresis measurements of super-lattices with (a) n = 1, 2, 4 and (b) n = 6, 8, 10 repetitions of the $Gd_{21}Co_{28}O_{51}$ PMA heterostructures. Solid lines correspond to the out-of-plane measurements and the dotted lines correspond to the in-plane measurements. The insets show the desired out-of-plane hysteresis behavior at low fields in the multi-repetition heterostructures. (c) Effective anisotropy energy density and anisotropy field as a function of the number of repetitions of the heterostructure unit-cell. The dashed line is for visualization of the increasing anisotropy field.

 $Si/SiO_2(3 \text{ nm})/Ta(3 \text{ nm})/Pt(3 \text{ nm})/Gd_xCo_{1-x}(t)/Pt(5 \text{ nm}) \text{ through}$ variations in composition, changes in reactive oxygen flow rates, and construction of multi-repetition heterostructures. Changes to the RE-TM ratio results in a magnetic compensation point for alloys with a composition between x = 28-32%, where the saturation magnetization approaches zero, and effective anisotropy energy density (K_{eff}) diverges around X_{M} . Temperature dependent magnetic properties show that Codeficient alloys with $x > X_{\rm M}$ have a compensation temperature $T_{\rm M} > 300$ K. An optimal oxygen flow rate of 0.5 sccm, which corresponds to a cation to oxygen (R:O) ratio of 1:1 is found to produce a strong PMA with a $K_{\rm eff} = 1 \times 10^5 {\rm erg \ cc^{-1}}$, an order of magnitude greater than alloys sputtered without oxygen. XPS analysis showed that Co oxidizes preferentially at higher oxygen flow rates leading to a Co-deficient stoichiometry of Gd₂₁Co₂₈O₅₁ and reduced saturation magnetization accompanying the stronger PMA. Lastly, through dipolar coupling in a multi-repetition heterostructure, a large effective anisotropy $(K_{\rm eff})$ of 2.13 imes 10⁵ erg cc⁻¹ and a giant anisotropy field $(H_{\rm K})$ of 11 kOe is achieved with 10 repetitions of the PMA heterostructure containing Gd₂₁Co₂₈O₅₁. Therefore, control of perpendicular magnetic anisotropy in ferrimagnetic Gd_xCo_{1-x} alloys using composition, oxygenation, and dipolar stacking will pave the way for integrated non-reciprocal devices in the upper-microwave/mm-wave bands and ultrafast high-density magnetic memory devices that approach switching speeds down to 30 ps.

Experimental

Sputter deposition of Gd_xCo_{1-x} PMA heterostructures

Thin films of Gd_xCo_{1-x} were co-sputtered from Gd and Co metallic targets from RF and DC magnetron sources, respectively, in a reactive ambient of argon (ultra-high purity, 99.999%) and oxygen (99.999%) at a process pressure of 3 mTorr. The base pressure was below 5×10^{-8} Torr. The sputtering power for Gd target was varied between 20-50 W, while maintaining the Co target at a constant power of 50 W. Oxygen flow rates were controlled using a mass flow controller (MFC) that has a range of 0.3-10 sccm with a resolution of 0.1 sccm. Argon flow rate was kept constant at 38 sccm. Other layers in the heterostructure such as Pt and Ta were sputter deposited from DC targets and SiO2 from an RF source. The deposition rates for the metallic and oxide species were predetermined using a crystal monitor, and thicknesses were verified by profilometer measurements using a KLA Tencor P-16 surface profilometer.

Structural and elemental characterization

Structural characterization of the Pt layers was carried out using a Rigaku SmartLab from a theta-two theta $(\theta - 2\theta)$ scan. The Pt (111) orientation observed at 39.6° was used to quantify the crystallinity of the thin film. The diffraction peak was verified by comparing it to the powder diffraction pattern 243678 for Pt from the Inorganic Crystal Structure Database (ICSD). Elemental composition was determined using an Oxford Instruments Ultim Max energy dispersive X-ray spectroscopy (EDS) detector in a Zeiss Gemini 500 scanning electron microscope (SEM). The beam was set to 20 keV and quantitative data processing was carried out in the Aztec Nanoanalysis software by Oxford Instruments. The atomic fractions reported in this work are an average of 9 measurements from different areas of the sample with an error margin of 5-8%.

Magnetic measurements

Magnetic hysteresis measurements (or M vs. H loops) were recorded using a Lake Shore Cryotronics 8600 Series vibrating sample magnetometer (VSM) at room temperature. The saturation magnetization (M_S) , remanent magnetization (M_R) and coercive field (H_C) were obtained from the MH loops. A maximum field of 1.5 T (or 15 kOe) was applied to each sample during measurement, and data from a narrow range of magnetic fields is presented for clarity, where applicable. Effective anisotropy energy densities are extracted from the difference in area under the anhysteretic M-H curves for the out-of-plane and in-plane measurements from the first quadrant. Anhysteretic curves are the average between the two magnetization curves in the first quadrant corresponding to field sweeps between 0 to 15 kOe and 15 kOe to 0 Oe.

Temperature-dependent magnetic property measurements were carried out in the VSM mode of a Quantum Design DynaCool physical property measurement system (PPMS). The sample was mounted in an in-plane geometry such that the magnetic field is parallel to the surface of the film. Temperature was swept from 100 K to 350 K in an applied field of 1400 Oe, sufficient to saturate the sample. A relatively low field for measurement was chosen to eliminate background noise from the substrate holder. Integration time for each measurement was increased for better sensitivity near the compensation region.

Oxygen quantification using surface probe analysis

Samples were analyzed using a Surface Science Instruments SSX-100 ESCA Spectrometer with operating pressure of 1×10^{-9} Torr. Monochromatic Al Kα X-rays (1486.6 eV) with a source size of 500 µm for the survey scans and depth profiles were used to collect photoelectrons from a 1×2 mm spot at the sample. Photoelectrons were collected at a 55° emission angle with source to analyzer angle of 70°. A hemispherical analyzer determined electron kinetic energy, using a pass energy of 150 eV for survey scans, and 50 eV for high resolution scans. The heterostructures were milled using an ion beam at an etch rate of 1.8 Å s^{-1} and measurements after 49 seconds of etching corresponded to center of the Gd_xCo_{1-x} layer. XPS data quantification - such as peak fitting, determining atomic percentage were conducted using CasaXPS. The line shape is an asymmetric Lorentzian (LA(α , β , m)), which is a convolution of Gaussian with a Lorentzian that produces asymmetric Voightlike profiles. The values α , β control the spread of the Lorentzian tail on either side of the peak maximum, giving rise to asymmetric profiles and m defines the width of the Gaussian

that is convoluted with the Lorentzian line shape. A line shape of LA(1.5, 243) is used to fit the Gd 4d, O 1s and Co loss peaks, while a line shape of LA(1.3, 5, 12) is used to fit the Co $2p_{3/2}$ peak that requires an asymmetric tail on one side of the peak maximum. All analyses are carried out with a Shirley-type background.

Author contributions

Description of author contributions based on CRediT (the Contributor Roles Taxonomy). K. S.: conceptualization, data curation, formal analysis, investigation, methodology, validation, visualization, writing – original draft, review & editing. Y. C., L. C.: investigation, resources, writing – review & editing. D. K. D., J. G. W.: investigation, formal analysis, resources, writing – review & editing. A. E.: conceptualization, funding acquisition, formal analysis, project administration, supervision, writing – original draft, review & editing.

Conflicts of interest

There are no conflicts to declare.

Acknowledgements

Part of this work made use of the Cornell Center of Materials Research Shared Facilities which are supported through the NSF MRSEC program (DMR-1719875) and the Cornell Nano-Scale Facility, a member of the National Nanotechnology Coordinated Infrastructure (NNCI), which is supported by the National Science Foundation (Grant NNCI-2025233). This material is based upon work supported by the National Science Foundation under Grant No. 2030207. Any opinions, findings, and conclusions or recommendations expressed in this material are those of the authors and do not necessarily reflect the views of the National Science Foundation.

References

- I. M. Miron, K. Garello, G. Gaudin, P. J. Zermatten, M. V. Costache, S. Auffret, S. Bandiera, B. Rodmacq, A. Schuhl and P. Gambardella, *Nature*, 2011, 476, 189–193.
- 2 X. Qiu, Z. Shi, W. Fan, S. Zhou and H. Yang, *Adv. Mater.*, 2018, **30**, 1705699.
- 3 Q. Shao, P. Li, L. Liu, H. Yang, S. Fukami, A. Razavi, H. Wu, K. Wang, F. Freimuth, Y. Mokrousov, M. D. Stiles, S. Emori, A. Hoffmann, J. Åkerman, K. Roy, J.-P. Wang, S.-H. Yang, K. Garello and W. Zhang, *IEEE Trans. Magn.*, 2021, 57, 1–39.
- 4 L. Cestarollo, K. Srinivasan and A. El-Ghazaly, *J. Magn. Magn. Mater.*, 2022, 169825.
- 5 J. Finley and L. Liu, Appl. Phys. Lett., 2020, 116, 110501.
- 6 Y. Chen, T. Sakai, T. Chen, S. D. Yoon, A. L. Geiler, C. Vittoria and V. G. Harris, *Appl. Phys. Lett.*, 2006, 88, 062516.
- 7 X. Wang, Y. Chen, H. Chen, Y. Gao, Y. He, M. Li, H. Lin, N. Sun and N. Sun, *Appl. Phys. Lett.*, 2018, **112**, 192903.

- 8 K. Srinivasan, C. Radu, D. Bilardello, P. Solheid and B. J. H. Stadler, *Adv. Funct. Mater.*, 2020, **30**, 2000409.
- 9 V. G. Harris, IEEE Trans. Magn., 2012, 48, 1075-1104.
- 10 J. Finley and L. Liu, Phys. Rev. Appl., 2016, 6, 054001.
- 11 H. Wu, Y. Xu, P. Deng, Q. Pan, S. A. Razavi, K. Wong, L. Huang, B. Dai, Q. Shao, G. Yu, X. Han, J.-C. Rojas-Sánchez, S. Mangin and K. L. Wang, *Adv. Mater.*, 2019, 31, 1901681.
- 12 R. Mishra, J. Yu, X. Qiu, M. Motapothula, T. Venkatesan and H. Yang, *Phys. Rev. Lett.*, 2017, **118**, 167201.
- 13 A. El-Ghazaly, B. Tran, A. Ceballos, C.-H. Lambert, A. Pattabi, S. Salahuddin, F. Hellman and J. Bokor, *Appl. Phys. Lett.*, 2019, 114, 232407.
- 14 A. El-Ghazaly, J. Gorchon, R. B. Wilson, A. Pattabi and J. Bokor, J. Magn. Magn. Mater., 2020, 502, 166478.
- 15 I. A. Campbell, J. Phys. F: Met. Phys., 1972, 2, L47-L50.
- 16 K. H. J. Buschow, J. Appl. Phys., 1980, 51, 2795-2798.
- 17 P. Hansen, C. Clausen, G. Much, M. Rosenkranz and K. Witter, J. Appl. Phys., 1989, 66, 756–767.
- 18 R. C. Taylor and A. Gangulee, J. Appl. Phys., 2008, 47, 4666.
- 19 K. Ueda, A. J. Tan and G. S. D. Beach, AIP Adv., 2018, 8, 125204.
- 20 L. Caretta, M. Mann, F. Büttner, K. Ueda, B. Pfau, C. M. Günther, P. Hessing, A. Churikova, C. Klose, M. Schneider, D. Engel, C. Marcus, D. Bono, K. Bagschik, S. Eisebitt and G. S. D. Beach, *Nat. Nanotechnol.*, 2018, 13, 1154–1160.
- 21 K. Cai, Z. Zhu, J. M. Lee, R. Mishra, L. Ren, S. D. Pollard, P. He, G. Liang, K. L. Teo and H. Yang, *Nat. Electron*, 2020, 3, 37–42.
- 22 J. Wang, C. Li, R. Tang, G. Chai, J. Yao and C. Jiang, *Appl. Phys. Lett.*, 2022, **120**, 102402.
- 23 K. Ueda, M. Mann, C.-F. Pai, A.-J. Tan and G. S. D. Beach, *Appl. Phys. Lett.*, 2016, **109**, 232403.
- 24 N. Roschewsky, C.-H. Lambert and S. Salahuddin, *Phys. Rev. B*, 2017, **96**, 064406.
- 25 T. Katayama, K. Hasegawa, K. Kawanishi and T. Tsushima, *J. Appl. Phys.*, 1978, **49**, 1759–1761.
- 26 J. Kim, D. Lee, K.-J. Lee, B.-K. Ju, H. C. Koo, B.-C. Min and O. Lee, *Sci. Rep.*, 2018, **8**, 6017.
- 27 S. Esho, J. Appl. Phys., 2008, 50, 1006.
- 28 A. Brunsch and J. Schneider, *J. Appl. Phys.*, 1977, 48, 2641–2643.
- 29 Y. Togami and K. Kobayashi, Jpn. J. Appl. Phys., 1981, 20, 1457.
- 30 A. Ceballos, A. Pattabi, A. El-Ghazaly, S. Ruta, C. P. Simon, R. F. L. Evans, T. Ostler, R. W. Chantrell, E. Kennedy, M. Scott, J. Bokor and F. Hellman, *Phys. Rev. B*, 2021, 103, 024438.
- 31 J. P. Hanton, IEEE Trans. Magn., 1967, 3, 505-509.
- 32 R. Dudric, G. Souca, K. Kuepper and R. Tetean, *Phys. Status Solidi B*, 2019, **256**, 1800320.
- 33 P. Terzieff and K. Lee, J. Appl. Phys., 2008, 50, 3565.
- 34 T. J. Chuang, C. R. Brundle and D. W. Rice, *Surf. Sci.*, 1976, **59**, 413–429.
- 35 M. C. Biesinger, B. P. Payne, A. P. Grosvenor, L. W. M. Lau, A. R. Gerson and R. S. Smart, *Appl. Surf. Sci.*, 2011, 257, 2717–2730.

- 36 K. Wandelt and C. R. Brundle, Surf. Sci., 1985, 157, 162-182.
- 37 Y. Zhang, L. Zhou, S. Tao, Y. Jiao, J. Li, K. Zheng, Y. Hu, K. Fang, C. Song, X. Zhong, L. Xu, K.-F. Yao, Z. Zhang and N. Chen, Sci. China Mater., 2021, 64, 2305-2312.
- 38 N. Chen, K. Fang, H. Zhang, Y. Zhang, W. Liu, K. Yao and Z. Zhang, J. Semicond., 2019, 40, 081510.
- 39 S. Bendson and J. Judy, IEEE Trans. Magn., 1973, 9, 627-631.
- 40 R. J. Gambino and J. J. Cuomo, J. Vac. Sci. Technol., 1978, 15, 296-301.
- 41 H. Fu, M. Mansuripur and P. Meystre, Phys. Rev. Lett., 1991, **66**, 1086-1089.
- 42 S. Iida, J. Phys. Soc. Jpn., 1967, 22, 1201-1209.
- 43 J.-L. Mattei, E. Le Guen, A. Chevalier and A.-C. Tarot, J. Magn. Magn. Mater., 2015, 374, 762-768.
- 44 Y. Zhu, Z. Zhang, B. Ma and Q. Y. Jin, J. Appl. Phys., 2012, 111, 07C106.
- 45 K.-F. Huang, D.-S. Wang, H.-H. Lin and C.-H. Lai, Appl. Phys. Lett., 2015, 107, 232407.